



The foehn effect during easterly flow over Svalbard

Anna A. Shestakova¹, Dmitry G. Chechin^{1,2}, Christof Lüpkes³, Jörg Hartmann³, and Marion Maturilli⁴

¹Air-Sea Interaction Laboratory, A.M. Obukhov Institute of Atmospheric Physics,
Russian Academy of Sciences, Moscow, 119017, Russia

²Moscow Center for Fundamental and Applied Mathematics, Leninskie Gory, 1, Moscow, 119991, Russia

³Alfred Wegener Institute, Helmholtz Centre for Polar and Marine Research, Bremerhaven, Germany

⁴Alfred Wegener Institute, Helmholtz Center for Polar and Marine Research, Potsdam, Germany

Correspondence: Anna A. Shestakova (shestakova@ifaran.ru)

Received: 7 June 2021 – Discussion started: 15 June 2021

Revised: 20 November 2021 – Accepted: 20 December 2021 – Published: 1 February 2022

Abstract. This article presents a comprehensive analysis of the foehn episode which occurred over Svalbard on 30–31 May 2017. This episode is well documented by multiplatform measurements carried out during the Arctic CLOUD Observations Using airborne measurements during polar Day (ACLOUD) and Physical feedbacks of Arctic PBL, Sea ice, Cloud And Aerosol (PASCAL) campaigns. Both orographic wind modification and foehn warming are considered here. The latter is found to be primarily produced by the isentropic drawdown, which is evident from observations and mesoscale numerical modeling. The structure of the observed foehn warming was in many aspects very similar to that for foehns over the Antarctic Peninsula. In particular, it is found that the warming was proportional to the height of the mountain ridges and propagated far downstream. Also, a strong spatial heterogeneity of the foehn warming was observed with a clear cold footprint associated with gap flows along the mountain valleys and fjords. On the downstream side, a shallow stably stratified boundary layer below a well-mixed layer formed over the snow-covered land and cold open water. The foehn warming downwind of Svalbard strengthened the north–south horizontal temperature gradient across the ice edge near the northern tip of Svalbard. This suggests that the associated baroclinicity might have strengthened the observed northern tip jet. A positive daytime radiative budget on the surface, increased by the foehn clearance, along with the downward sensible heat flux provoked accelerated snowmelt in the mountain valleys in Ny-Ålesund and Adventdalen, which suggests a potentially large effect of the frequently observed Svalbard foehns on the snow cover and the glacier heat and mass balance.

1 Introduction

The observed climate change in the Arctic is strong, although the mechanisms are not yet fully understood (Serreze and Barry, 2011; Dethloff et al., 2019). In some regions the climatic signal is strongly modulated by the orography, as is the case in Svalbard (Beine et al., 2001; Argentini et al., 2003; Kilpeläinen and Sjöblom, 2010; Kilpeläinen et al., 2011). To better extract the climatic signal from the observational time series, one needs to study the orographic effects and their dependence on the parameters of the large-scale flow. The focus of this study is on the orographic winds observed during foehn, namely, downslope windstorms, gap flows and tip

jets, and their impact on the lower atmosphere and the surface heat budget.

There are several reasons why it is important to investigate these winds in more detail. First, the Fram Strait is one of the “hot” spots of the Arctic climate system: Atlantic water experiences transformation as it flows into the Arctic while sea ice is being exported through the Fram Strait, where it melts or forms (during cold-air outbreaks). These processes can be affected by orographic winds due to the influence of the latter on the momentum and heat transport between atmosphere and ocean as well as on the heat budget of the sea ice surface, including that in fjords. According to model results (Kilpeläinen et al., 2011), values of turbulent heat fluxes can

reach up to 500 W m^{-2} for sensible heat and 300 W m^{-2} for latent heat over the wintertime ice-free sea surface in Isfjorden (Svalbard), even during moderate easterly foehn winds.

Another crucial component of the climate system, which is affected by the orographic winds, is the energy exchange between the atmosphere and glacier surfaces. A high frequency and intensity of foehns can lead to an increased melting of glaciers. This is well documented for Antarctica, where foehn has a strong effect on the mass balance of glaciers and sea ice in the Antarctic Peninsula region (Elvidge et al., 2015; Turton et al., 2018; Elvidge et al., 2020).

Finally, orographically induced winds and turbulence are often strong and represent danger for aviation and other human activities. Heterogeneity of the orographic winds, i.e., the occurrence of strong jets and wakes, can be so strong in the Svalbard fjord areas that it poses danger to small vessels (Barstad and Adakudlu, 2011). Also, it is documented that downslope windstorms to the west of Svalbard cause ship icing (Samuelsen and Graversen, 2019).

Such strong windstorms frequently occur on the western slopes of Svalbard with a prevailing large-scale easterly flow and are mentioned in many articles (e.g., Dörnbrack et al., 2010; Kilpeläinen et al., 2011; Mäkiranta et al., 2011; Beine et al., 2001; Maciejowski and Michniewski, 2007; Mięgała et al., 2008; Láska et al., 2017). Using idealized modeling and aircraft observations, Dörnbrack et al. (2010) investigated an easterly flow over Svalbard and found that gap flows and tip jets have an impact on the boundary-layer structure and aerosol concentrations. However, downslope windstorms over Svalbard and especially the foehn effect have not yet been well documented. Mostly, only the near-surface observations and the associated large-scale circulation are discussed in relation to the Svalbard foehns, while the three-dimensional analysis of this phenomenon is missing.

In addition to downslope windstorms, other local winds are considered in this paper. Gap winds are directed along the fjords and usually spread far from the obstacle if the gap is not too narrow and the Froude number is not too small (Gaberšek and Durran, 2004). Tip jets at the southern and northern edges of the archipelago can be quite strong (Reeve and Kolstad, 2011; Sandvik and Furevik, 2002) and lead to significant changes in heat fluxes over the sea surface, similarly to the well-known southern Greenland tip jets (Doyle and Shapiro, 1999; Renfrew et al., 2009; Outten et al., 2009).

The main difference between the listed winds lies in their nature, i.e., in the physical mechanism of their formation. Under the action of a pressure gradient, air flows into the gaps (during gap winds) or around an obstacle (during tip jets), stream lines converge, and velocity increases (Markowski and Richardson, 2011). When the air at least partially overflows the obstacle, a downslope windstorm may occur. If this is the case, convergence of stream lines on the leeward side occurs due to (i) the transition of the flow to the supercritical state and/or (ii) breaking of high-amplitude internal gravity waves over the mountains. Downstream, a

hydraulic jump (a jump-like change in the flow thickness) usually occurs, and the flow becomes subcritical, where a calm zone (wake) is formed (Durran, 1990). Evidences of wake formation downstream of northwestern Spitsbergen was found in many simulations of airflow over Svalbard (e.g., Skeie and Grønås, 2000; Sandvik and Furevik, 2002; Dörnbrack et al., 2010; Reeve and Kolstad, 2011). Despite the existing knowledge on the orographic flows, their local features need to be studied for each particular region because the complex local orography and surface conditions may lead to a co-existence and interaction of several flow types and regimes.

Foehn winds are particularly important because they are associated with two effects: (i) downslope windstorm and (ii) foehn warming. Numerous studies of foehns in different regions have focused primarily on the dynamics of the downslope winds (e.g., Brinkmann, 1974; Hoinka, 1985; Skeie and Grønås, 2000; and many others). However, Elvidge and Renfrew (2016) and Elvidge et al. (2016) draw attention to the detailed structure of foehn warming downwind of the Antarctic Peninsula and its effect on the ice shelf melt. Previous investigations of foehns have also addressed this issue (e.g., Seibert, 1990; Olafsson, 2005; Steinhoff et al., 2013) but were not as detailed and comprehensive. Elvidge and Renfrew (2016) list the following mechanisms which produce the foehn warming: (1) isentropic drawdown, (2) turbulent sensible heating (mechanical downward mixing of warmer air in the stratified flow), (3) radiative heating (due to the cloud-free conditions on the lee side of the mountains), and (4) latent heat release and precipitation mechanism. They showed that the prevailing mechanism depends on the Froude number of the flow (i.e., wind speed and stratification) as well as the moisture content of the incoming flow and that several mechanisms can act simultaneously. The goal of our study is also to document the structure of foehn warming and its effect on the surface heat balance but in a region with more complex orography as compared to the Antarctic Peninsula. The latter is called by Elvidge et al. (2016) “an excellent natural laboratory” to study foehns due to the almost two-dimensional structure of the mountain ridge there.

Thus, the goal of this paper is to document in detail the orographic modification of the flow and of the atmospheric boundary layer during easterly flow over Svalbard. Our focus is on studying the foehn effect from in situ observations and its impact on the boundary layer and heat balance in the surface layer. To that aim, we used a unique set of observations on 30–31 May 2017 collected during the aircraft campaign Arctic CLOUD Observations Using airborne measurements during polar Day (ACLOUD) and the shipborne campaign Physical feedbacks of Arctic PBL, Sea ice, Cloud And Aerosol (PASCAL) (Wendisch et al., 2019). Also, we used observations from Ny-Ålesund, Svalbard, where the frequency of radiosoundings operated by the AWIPEV research base was increased to four launches per day in connection to the ACLOUD/PASCAL campaigns. Using this set of obser-

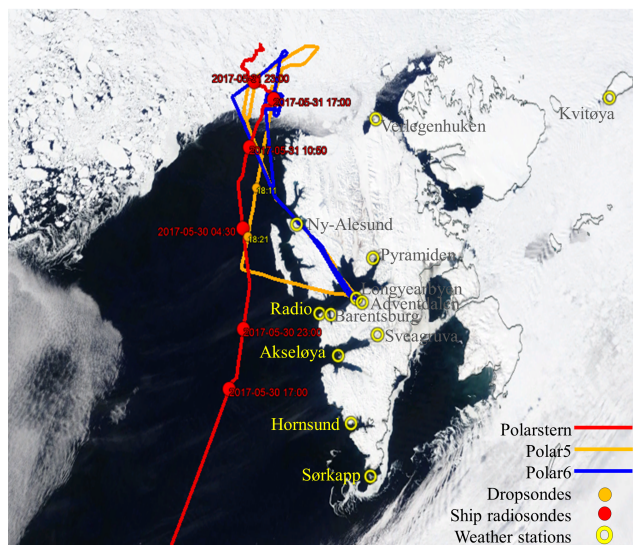


Figure 1. Satellite visible image (MODIS-corrected reflectance from NASA Worldview, <https://worldview.earthdata.nasa.gov>, last access: 25 January 2022) of the study area at $\sim 12:00$ UTC, 31 May 2017. Lines and points show ship and aircraft tracks, locations of dropsondes and radiosonde launches, and weather stations on Svalbard.

vations, we aimed to gain better understanding of the strength and structure of the orographic modification of the flow. We also used high-resolution simulations of the Weather Research and Forecasting (WRF) model to obtain a better three-dimensional view of the orographic impact on the flow.

The structure of the paper is as follows. Section 2.1 describes the observations. The setup of numerical simulations with WRF is presented in Sect. 2.2. The synoptic background of the considered episode is described in Sect. 3.1. Section 3.2–3.4 are devoted to the structure of the orographic winds and foehn warming. In Sect. 3.5, the effect of foehn on the surface heat budget over the snow-covered surface is considered. The main results are summarized in Sect. 4.

2 Data and methods

2.1 Observations

We investigated a period of increased wind velocities and air temperature over the western part of Svalbard, which occurred on 30–31 May 2017 during large-scale easterly flow. Complex observations in the boundary layer were performed during this episode, including in situ surface-based observations, aircraft and ship observations, and vertical profiles obtained from dropsondes and radiosondes launched from ship and over land (in Ny-Ålesund). Automatic weather station (AWS) data were available in addition to standard observations at Ny-Ålesund, Longyearbyen and Barentsburg stations. Figure 1 shows only those stations whose observations were used in this article. Figure 1 also shows the track of the

research vessel (RV) *Polarstern* (Knust, 2017; Wendisch et al., 2019) and the locations of the ship radiosonde and aircraft dropsonde launches as well as the aircraft tracks (aircraft *Polar 5* and *Polar 6*). Information about the observations used is summarized in Table 1.

The two research aircraft of the German Alfred Wegener Institute (AWI), *Polar 5* and *Polar 6*, were involved in the ACLOUD campaign. Identical sets of meteorological sensors were installed on both aircraft, including five-hole probes and open-wire platinum temperature sensors for turbulence observations (Ehrlich et al., 2019b). Both aircraft conducted their flights on 31 May during the foehn episode. They performed a series of ascents and descents through the boundary layer on the downwind and thus western side of northern Svalbard, as well as vertical stacks of horizontal legs over the sea ice in the Fram Strait. Only the vertical profiles of temperature, humidity, wind speed and wind direction obtained from the aircraft ascents and descents were used in this study. A more detailed description of metadata and a summary of the aircraft and shipborne observations can be found in Wendisch et al. (2019) as well as Ehrlich et al. (2019b), and a description of the synoptic situation during ACLOUD is given in Knudsen et al. (2018).

To evaluate the foehn effect on the surface heat budget we used measurements of wind speed and direction, air temperature, and relative humidity, which are available from two masts with instrumentation at 2 and 10 m above the ground level (a.g.l.) (Table 1). One of the masts is along Kongsfjord located on the Ny-Ålesund measurement field and another one is in Adventdalen (station of the University Centre in Svalbard, <http://158.39.149.183/Adventdalen/index.html>, last access: 25 January 2022). The observations of both masts are representative of conditions in fjord valleys. These valleys have approximately the same width and are elongated from northwest to southeast.

The YOPP (Year of Polar Prediction) analysis of ECMWF (European Centre for Medium-Range Weather Forecasts) (<https://apps.ecmwf.int/datasets/data/yopp/levtype=sfc/type=cf/>, last access: 25 January 2022) with a spatial resolution of 0.25° was used for the analysis of the synoptic situation during the studied foehn episode.

2.2 Numerical modeling

The considered foehn episode was simulated using the mesoscale model WRF-ARW version 3.4.1. The model settings and the domain configuration were the following. We used three nested domains (with two-way nesting) centered on Svalbard: domain 1 with 80×80 nodes and grid spacing of 20 km, domain 2 with 181×201 nodes and grid spacing of 4 km, and domain 3 with 226×457 nodes and grid spacing of 1.3 km. Such grid spacing in domain 3 allows foehn to be adequately reproduced in areas with complex topography, as shown by Elvidge et al. (2015). The number of vertical levels was 40 with a vertical grid spacing of about 150 m

Table 1. Observations during foehn episode.

Type of observation	Location	Temporal resolution	Temporal coverage	Vertical resolution and/or height of measurements
Surface meteorological observations	Ny-Ålesund Barentsburg Adventdalen Longyearbyen and other stations (Fig. 1)	1 min 3 h 1 s, 20 Hz 1 h	Whole episode	Main meteorological parameters: 2 m a.g.l., wind 10 m a.g.l.
Surface radiation	Ny-Ålesund	1 min	Whole episode	2 m a.g.l.
Gradient masts	Ny-Ålesund Adventdalen	1 min 1 s	Whole episode	2 m and 10 m a.g.l.
Ship in situ observations	See Fig. 1	1 min	12:00, 30 May– 12:00, 31 May	Main meteorological parameters: 29 m a.m.s.l., wind 39 m a.m.s.l.
Radiosounding	Ny-Ålesund	6 h	Whole episode	Vertical resolution ~ 5 m
Ship radiosounding	See Fig. 1	6 h	12:00, 30 May– 12:00, 31 May	Vertical resolution ~ 20–30 m
Aircraft in situ observations	<i>Polar 5</i> <i>Polar 6</i> (see Fig. 1)	1 s	~ 15:00–19:00, 31 May	Height of observations 0– 3.7 km
Drosondes (<i>Polar 5</i>)	See Fig. 1	–	31 May (18:11, 18:21)	Vertical resolution ~ 5–10 m, height of observations 0–3.3 km

in the lowest 1 km. Radiative transfer was parameterized using the RRTMG scheme (Iacono et al., 2008). Vertical turbulent transfer was parameterized using the MYNN 2.5 scheme (Nakanishi and Niino, 2009). The simulations used the Noah land surface model and the Kain–Fritsch scheme for convection (only in the outer domain). The Global Forecast System (GFS) final analysis (FNL) with a 1° resolution was used as initial and boundary conditions. The model was initialized on 30 May at 00:00 UTC, and the numerical experiment lasted over 54 h, till 1 June, 06:00 UTC. The output interval was set to 1 h.

3 Results

3.1 Synoptic background

Easterly and northeasterly winds are rather common over Svalbard. Most cases of strong easterly winds over Svalbard are caused by Atlantic cyclones, when they become stationary to the west of Svalbard or when they are moving from west to east across the Barents Sea (Migała et al., 2008; Shestakova et al., 2020). The episode on 30–31 May 2017 occurred in a rather unusual synoptic situation, described in detail in Knudsen et al. (2018). A combination of the cyclone over the Barents Sea (which moved there from the

Kara Sea) and an anticyclone over Greenland led to an intensification of the northeasterly flow over the archipelago. The advection of a relatively warm air mass occurred in the northern part of the cyclone (Fig. 2). The air temperature at 850 hPa exceeded 0 °C upwind of Svalbard; however, it will be shown further that the near-surface temperature there was below zero (i.e., in equilibrium with the cold underlying surface) and the atmospheric boundary layer (ABL) was capped by an inversion.

The considered episode was preceded by relatively cold weather marked by several episodes of an off-ice northerly flow (Knudsen et al., 2018). In this preceding period, the air temperature in Ny-Ålesund oscillated around −5 °C. On 29 May, an abnormally warm period began, when the air temperature was higher than its long-term mean (Knudsen et al., 2018). With a strong easterly and northeasterly wind, the air temperature steadily increased and reached a maximum of about 7 °C on 31 May. At the beginning of the episode, the vertically integrated water vapor was rather high due to the preceding large-scale moisture advection (Knudsen et al., 2018). Later on 30 May, it began to decrease along with the relative humidity, reaching its minimum on 31 May in the morning. This humidity decrease was associated with the change in the large-scale flow direction from easterly to northeasterly (see Fig. B1d) and the advection of

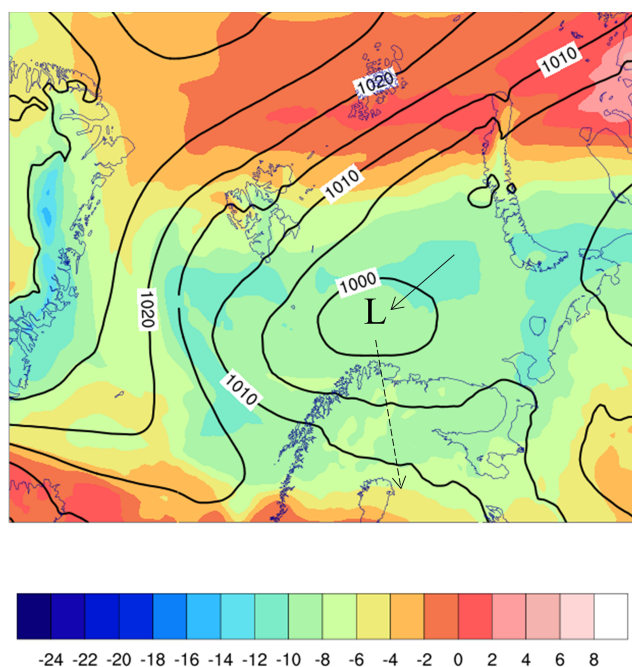


Figure 2. Synoptic chart at 06:00 UTC, 30 May 2017, according to ECMWF YOPP analysis: sea-level pressure (black contours, every 5 hPa) and air temperature at the 850 hPa level (color, every 2 K). Arrows show movements of the cyclone center during 29–31 May.

a less humid air mass. Also foehn might have contributed to the decreased humidity, as is usually observed during foehns (e.g., Hoinka, 1985; Seibert, 1990; Elvidge et al., 2016).

Wind speed near the surface was rather high as compared to average conditions but lower than during some documented downslope windstorms (Shestakova et al., 2018, 2020). The 10 min averaged wind speed attained the values of $15\text{--}20\text{ m s}^{-1}$ at 10 m a.g.l., and gusts attained 24 m s^{-1} at the Adventdalen and Hornsund stations. In Ny-Ålesund, the wind speed did not exceed 9 m s^{-1} , which is less than the 50th percentile of the wind speed during windstorms at this station (Shestakova et al., 2020). Significant fluctuations (“gustiness”) in all meteorological parameters were evident from measurements with a high temporal resolution on the *Polarstern* (Fig. 3) and at the Adventdalen station (not shown) and were especially pronounced in temperature and humidity. Such fluctuations are typical of downslope windstorms (e.g., Klemp and Lilly, 1975; Belusic et al., 2004; Efimov and Barabanov, 2013; Shestakova et al., 2018).

3.2 Spatial distribution of foehn warming

At first sight, the observed warming and air drying in Ny-Ålesund and downwind (at the *Polarstern* location) (Fig. 3) could be explained by the large-scale advection of a warmer and drier air mass. However, a closer examination of temperature (relative humidity) observations from different locations pointed out that the large-scale synoptic near-surface

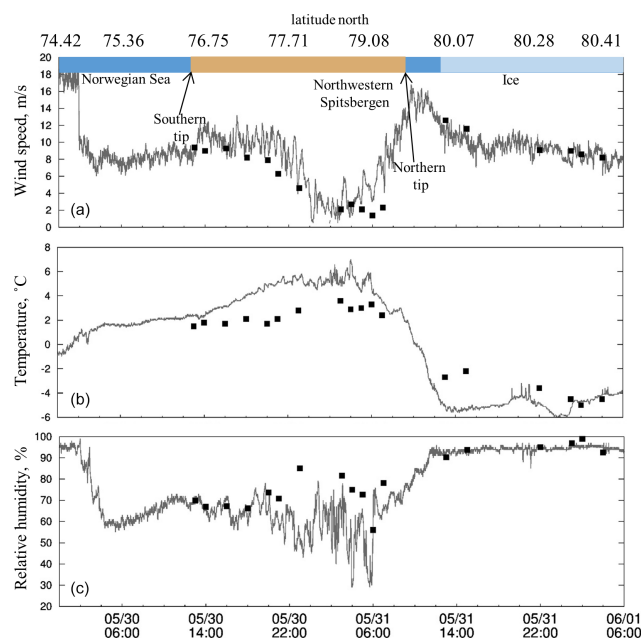


Figure 3. Wind speed (a), air temperature (b) and relative humidity (c) measured on RV *Polarstern* on 30–31 May 2017. Black squares show modeling data at the grid points nearest to the *Polarstern* track. Color panels on the top show when RV *Polarstern* was in the open sea (blue), downwind of Svalbard (brown) and in the sea ice (light blue).

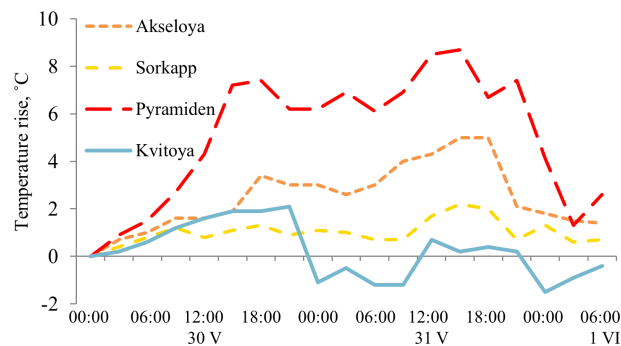


Figure 4. Temperature change from “initial” time at each individual AWS station during foehn episode, where the initial time is 00:00 UTC, 30 May.

warming (drying) was rather weak, but it was amplified by the orography at the locations downwind of the major mountain ridges.

Weather stations can be divided into four categories: (1) upwind (Kvitøya), (2) located on capes (Sørkapp on the southern cape and Verlegenuken on the northern cape), (3) influenced mainly by gap winds (such as Akseløya), and (4) influenced mainly by downslope windstorms (foehns) (such as Pyramiden, Ny-Ålesund, Longyearbyen). Category 1 and 2 stations are located on a rather flat terrain, at 8–10 m above mean sea level (a.m.s.l.).

Figure 4 shows the temperature rise, which is the difference between the observed temperature and the temperature at the initial time (00:00 UTC, 30 May), at stations of different categories (one from each category). Here, we used the temperature rise as a measure of the foehn warming as it allowed us to estimate in a simple way the warming from the ground-based observations. The drawback of this metric is that it does not accurately distinguish between foehn and non-foehn (air-mass advection, local radiative heating, etc.) warming. Note that Elvidge and Renfrew (2016) used a different measure of the foehn warming. Namely, they define the latter as the difference in temperatures at the same height downwind of the ridge and in the undisturbed flow upwind of the ridge.

A weak warming reaching only 2 °C at its maximum was observed at stations of the first and the second categories, as can be clearly seen from Figs. 4 and 5a. The latter figure shows the maximum temperature rise during the foehn episode.

On the contrary, the stations on the downwind side of Svalbard showed much stronger warming. Figure 4 shows that in Pyramiden (20 m a.m.s.l.), the temperature rise reached 9 °C, which is 5–8 times greater than the temperature rise at the Sørkapp station and presumably was caused by the foehn effect. Some stations showed a moderate temperature increase, such as the Akseløya station (20 m a.m.s.l.). There, the temperature rise amounted to about 4–5 °C (Fig. 4). A weaker temperature rise at Akseløya could be due to two reasons: first, there was a weaker foehn effect upwind of this station where the flow was passing through the gap along the Bellsund fjord (where Akseløya is located); second, there is a noticeable distance from the nearest upwind mountain ridge and the foehn warming could decrease due to the heat exchange with the colder surface of the fjord. Interestingly, the greatest temperature rise in Pyramiden was accompanied by the lowest wind speed among other stations (Fig. 5b). The latter is associated with a wake formation. The distribution of the relative humidity decrease is not shown, but this decrease was maximal at the stations with the maximal temperature rise, i.e., at the stations influenced by foehn.

Figure 6 shows that the differences in the magnitude of the foehn warming on the leeward side can be explained by the differences in the nature of the two observed orographic winds: the downslope windstorm and the gap wind. Vertical cross-sections are shown for the gap flow in Bellsund fjord (Fig. 6c and d) and for the downslope windstorm that occurs next to this fjord (Fig. 6e and f) over southern Svalbard. Concerning the downslope windstorm, a jet stream (area of high wind speed near the feet of lee slopes) descended almost to the surface (Fig. 6e). The height with the maximum wind velocity is 150–200 m, and the thickness of the jet was about 500 m, which is consistent with radiosoundings in Ny-Ålesund and aircraft in situ measurements in Longyearbyen region (not shown). An area of low winds occurred above the jet, most likely associated with gravity wave breaking. This

can be seen from the local instability that occurred here (in Fig. 6e, the red dots indicate regions where the Richardson number is smaller than 0.25). Jet streams associated with the downslope winds did not propagate far from the lee slopes (Fig. 6a and e). Wind speed near the surface was sharply attenuated, and the wake formed in the boundary layer. This wind stagnation in the wake can be clearly seen from *Polarstern* data and was well reproduced by the WRF model (Fig. 3). The abrupt wind speed change was due to the so-called hydraulic jump (Fig. 6e). Beneath the hydraulic jump, local instability occurred (Fig. 6e), which indicated the so-called boundary-layer separation (Markowski and Richardson, 2011). According to long-term observations (Maturilli et al., 2013), the Ny-Ålesund site on the western coast of Svalbard is characterized by the predominance of low wind speed (partly due to the wake formation), although the whole Atlantic sector of the Arctic is characterized by high wind speed (Hughes and Cassano, 2015). The combination of high-speed areas near the mountains and wakes downstream is typical of other downslope windstorms, e.g., for the Novaya Zemlya bora (Efimov and Komarovskaya, 2018) and Novorossiysk bora (Shestakova et al., 2018), which is not the case for gap flows. The latter propagated far into the sea with wind speed gradually decreasing (Fig. 6a and c).

The vertical cross-sections of the gap flow (Fig. 6c) show that wind amplification in them was rather small as compared to the incoming flow and the vertical air displacement was small too. The latter can be seen from the small difference in height of the lower isotherms between the windward and leeward sides of the mountains.

Although gap winds on Svalbard had a similar vertical scale and magnitude to downslope winds, differences in their spatial and vertical distribution formed a spatially heterogeneous structure of the warming. Downslope winds had a warming effect on the entire lower troposphere (Fig. 6f). This was due to the large-scale lowering of the isentropes (the so-called “isentropic drawdown”; Elvidge and Renfrew, 2016) over the Svalbard mountains while relatively cold air in the lower layers remained blocked on the upwind side of the mountains. Such a “warm footprint” of downslope winds extended far enough into the sea, as can be seen in Fig. 6b, and was also found in many previous studies (e.g., see Fig. 9 in Dörnbrack et al., 2010). Warm foehn air reached *Polarstern* (Fig. 3), which passed 50–100 km from the coast. On the contrary, gap winds and tip jets could attain high speed over the sea but had an insignificant effect on the near-surface temperature (Fig. 6d); therefore, gap winds produced “cold footprints” (compared with ambient air, warmed by downslope winds) on the temperature map (Fig. 6b). A similar cold footprint of gap flows was reported earlier by Elvidge et al. (2015). Nevertheless, adiabatic air heating over the archipelago was present in the gap flow too, but it was much weaker compared to that in the downslope winds and almost does not affect the surface layer (see point 3 in Fig. 7). There-

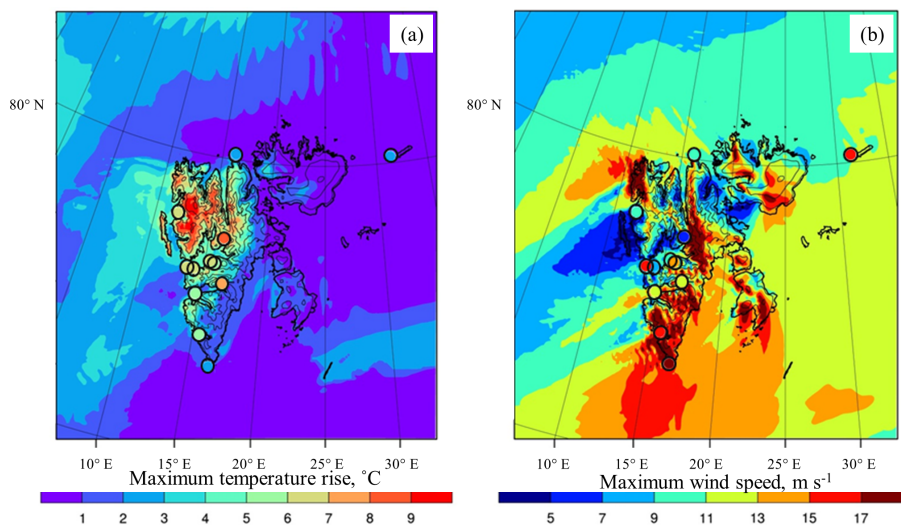


Figure 5. Maximum temperature rise at 2 m a.g.l. (see explanations in the text) (a) and maximum wind speed at 10 m a.g.l. (b) during the foehn episode according to modeling and observations at weather stations (circles).

fore, it was called a “dampened foehn effect” by Elvidge and Renfrew (2016).

Foehn warming caused by downslope winds was not homogeneous on different parts of the archipelago due to the different heights of the mountains. According to the WRF modeling, the maximum temperature rise as well as the maximum temperature difference between the downstream and upstream sides of the archipelago (up to 10 °C) occurred over northwestern Svalbard (Fig. 5). This is obviously due to the larger number and larger height of mountain ridges there compared to southern Svalbard. In the northern part, the mountain ridge heights reach up to 1000–1300 m, while in the southern part they reach only 500–800 m. The presence of a warmer air mass aloft is clearly seen in the model’s inflow profiles (Fig. 7a) where an elevated inversion was present with a base at about 700 m height, which is below the mountain top height. As a result, warm air from the inversion layer descended to the surface on the leeward side experiencing adiabatic heating (mechanism no. 1 from the Introduction) as shown by the modeled profile 2 in Fig. 7a. Vertical cross-sections of potential temperature across northern (not shown) and southern (Fig. 6) Svalbard revealed that the air near the surface on the lee side of mountains originated from the height approximately corresponding to the maximum mountain height (if we assume that the isentropes coincide with the stream lines). The difference in potential temperature between the maximum mountain height and the earth surface in the incoming flow (profile 1 in Fig. 7) corresponds to a temperature rise due to the isentropic drawdown (Elvidge and Renfrew, 2016). It amounted to about 7–10 K for northern Svalbard and to about 2–4 K for southern Svalbard, which is close to the temperature rise shown in Fig. 5. Another possible and additional process is the increased turbulent mixing (mechanism no. 2 from the Introduction) over

the complex orography of northern Svalbard transporting the warmer air downwards. Radiative air heating (mechanism no. 3 from the Introduction) could also have occurred in our case. Starting from the afternoon on 30 May, there were no clouds on the lee side of the mountains (as observed from the satellite images; see Fig. 1) due to foehn clearance. According to the WRF simulation, precipitation on the windward side of the mountains appeared only at the very beginning of the episode and its amount was negligible; therefore, we conclude that the contribution of the latent heat release mechanism (no. 4 from the Introduction) was small in the studied case.

3.3 Boundary-layer structure

In this section, we investigated the observed temperature structure of the lower troposphere during foehn in more detail with a special focus on the atmospheric-boundary-layer response to the foehn warming. Namely, we compared the observed and simulated vertical temperature profiles downwind of Svalbard, which were affected by foehn, with those in the undisturbed flow upwind of Svalbard and over the sea ice to the north of Svalbard.

First of all, let us consider the east–west potential temperature cross-section (i.e., along the trajectories) during foehn. Figures 7 and 8 show the potential temperature profiles observed (or simulated) upwind, over Svalbard and over water downwind. The simulated upwind profiles were well mixed up to the height of about 600 m with a mixed-layer temperature of about 269.5 K. Over Svalbard, as observed by the radiosoundings in Ny-Ålesund, a much warmer mixed layer formed during the considered foehn event. Its height varied from about 700 to 500 m, and the mixed-layer temperature was about 276 K. A more detailed analysis of the pro-

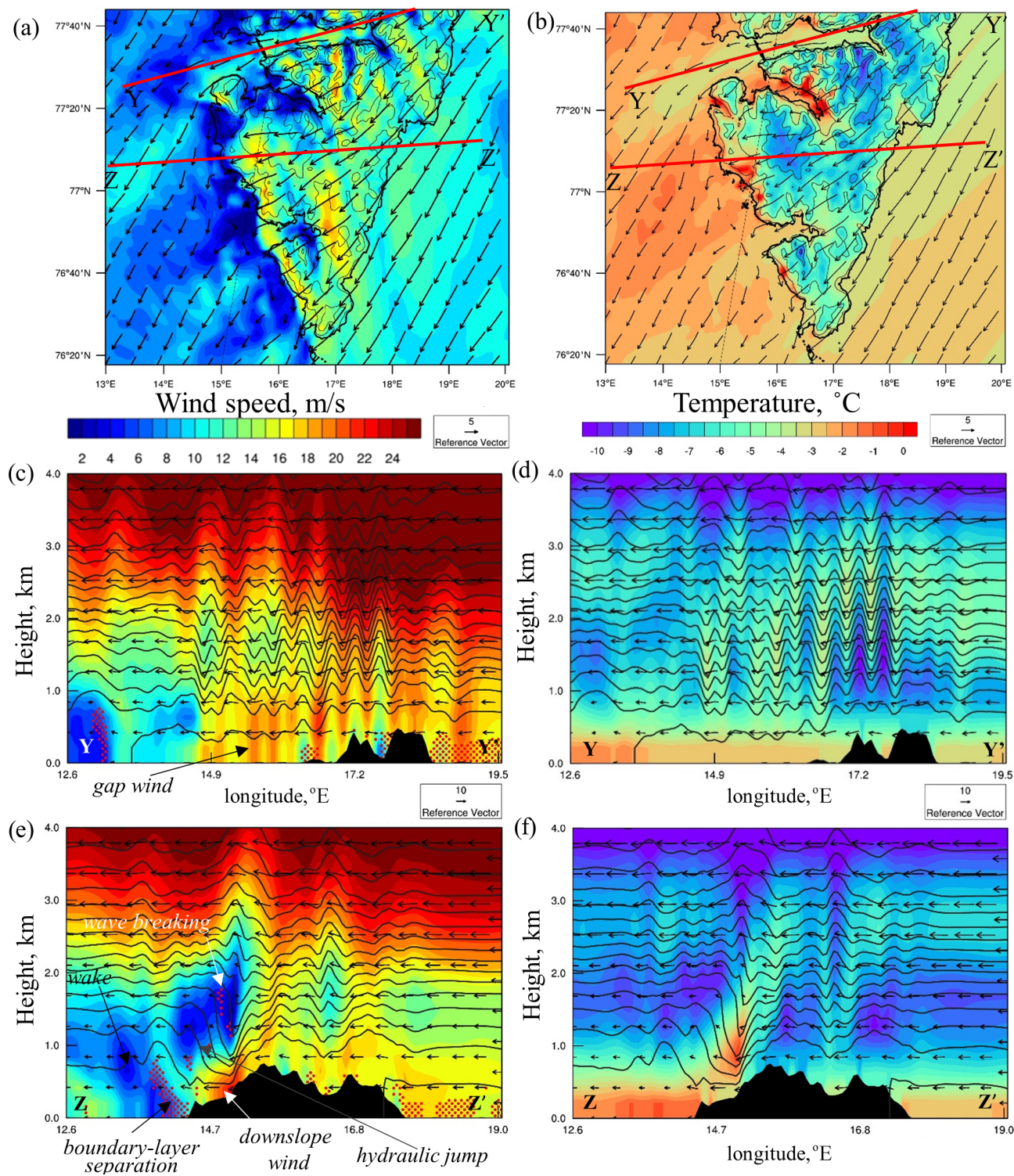


Figure 6. Wind speed (a, c, e) and air temperature (b, d, f) maps (a, b) and cross-sections along the northern line Y–Y' (c, d) and the southern line Z–Z' (e, f) at 12:00 UTC, 30 May 2017, according to modeling results. Arrows show wind vectors; red dots in the wind speed cross-sections mark regions with $Ri < 0.25$.

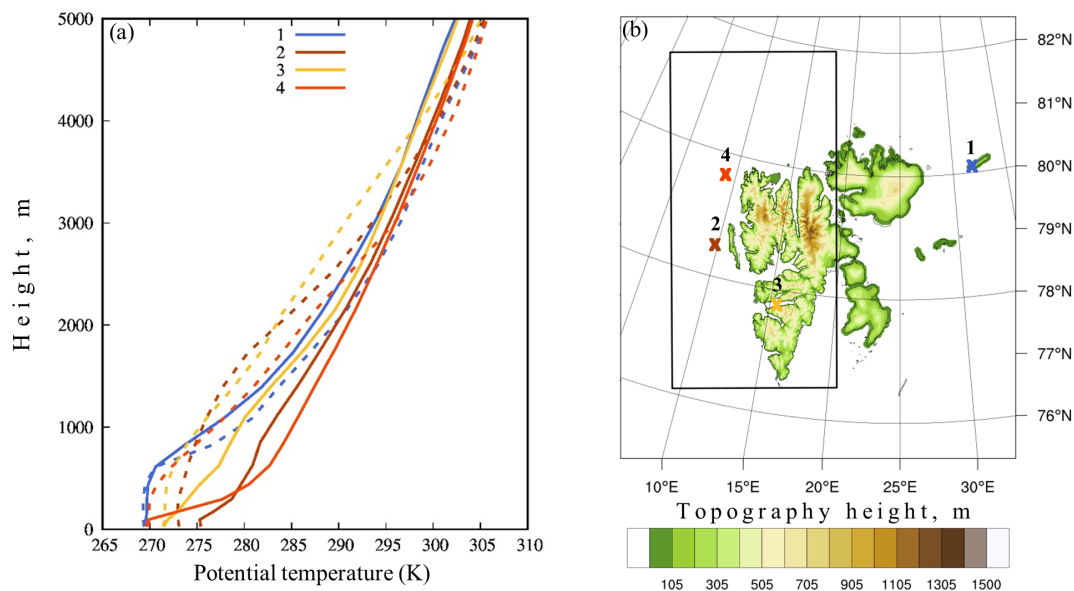


Figure 7. (a) Vertical profiles of potential temperature in points 1–4 upstream and downstream of Svalbard at the beginning (06:00 UTC, 30 May 2017, dashed lines) and in the middle of the foehn episode (06:00 UTC, 31 May 2017, solid lines) according to modeling results and (b) map of nested model domains 2 and 3 showing the locations of points 1–4 (X marks) and topography height (color).

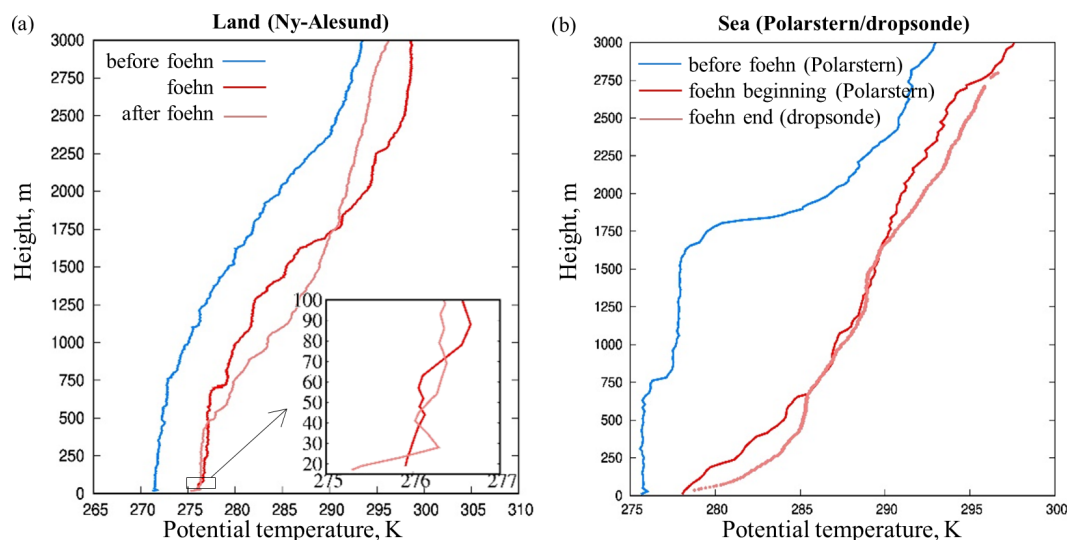


Figure 8. Observations of potential temperature in the lower troposphere (a) over land (Ny-Ålesund) and (b) over sea. (a) Radiosonde observations over Ny-Ålesund before foehn onset (12:00 UTC, 29 May), during foehn (12:00 UTC, 30 May) and after foehn episode (12:00 UTC, 1 June). The lowermost 100 m layer is enlarged (see inset). (b) *Polarstern* radiosonde observations at 11:00, 30 May (south from Spitsbergen) and at 04:34, 31 May, and dropsonde observations at 18:21, 31 May. The latter two observations were taken in front of northwestern Spitsbergen, at the beginning and at the end of foehn episode, respectively.

files over Ny-Ålesund shows that the lowermost 100 m thick layer was stably stratified (Fig. 8a). This is not surprising because the land surface was covered with snow whose temperature was at the melting point, i.e., colder than the overlying air. Surface-layer observations at Ny-Ålesund also confirmed stable stratification resulting in a downward (negative) turbulent heat flux, as shown further in Sect. 3.5.

Further downwind, over the open water, the whole air column and especially the lowest 300–400 m layer were stably stratified (Fig. 8b). The potential temperature at 500 m height is 285 K, i.e., much warmer than over Ny-Ålesund and upwind of Svalbard, while the surface temperature of open water was close to 275–277 K according to the YOPP analysis of ECMWF. In the lowest 500 m the low-level temperature

inversion was very strong with a vertical gradient of potential temperature of about 1.5 K per 100 m according to the dropsonde data.

Inside the gap flow (point 3 in Fig. 7), temperature stratification above the water was also stable, but the vertical temperature gradient was approximately 2 times less than at point 2 (Fig. 7). Approximately the same but slightly weaker stratification was found by Dörnbrack et al. (2010) inside the gap flow in Isfjorden. This difference between points 2 and 3 is associated, firstly, with a greater foehn heating at point 2 (as mentioned above) and, secondly, with a lower wind speed and therefore less mixing in the wake compared with the gap flow area.

Figures 7 and 8 also show potential temperature profiles before and during the foehn episode. Enhanced low-level warming during foehn and a transition from a well-mixed to a more shallow and stably stratified boundary layer were especially evident over water and the ice edge downwind of northern Svalbard.

More detailed observations of the vertical thermal structure downwind of northern Svalbard were obtained during the ascents and descents of *Polar 6* along its track towards the north (Fig. 9). The profile over the open water T2, which is closest to the downwind side of the mountains, clearly shows the result of downward propagation of warm and dry air from aloft to the heights of about 70 m. The observed air temperature at that height reached 10 °C. Below that height a very shallow and strongly stable boundary layer formed over cold water. Further north and away from the mountains both wind speed and the height of the stable boundary layer (profiles T3 and T4) increased. Over the rough sea ice, a cold, moist and well-mixed boundary layer was observed with its height increasing to the value of about 300 m in the north (profiles T6–T8). The potential temperature in the mixed layer over sea ice decreased to about −7 °C and was in equilibrium with the sea ice surface temperature. The mixed layer was capped by a strong inversion with a temperature jump of about 10 K. Unlike directly downwind of the mountains, where the foehn effect was evident, it is hard to conclude whether this warm and dry air above the boundary layer over ice was advected by the large-scale flow or to some extent also affected by foehn.

The described temperature profiles (Fig. 9a) show a strong north–south horizontal temperature gradient in the lowest layer. Although the horizontal temperature gradient was mostly due to the ice–water surface temperature difference, it was clearly enhanced by foehn. Also, a sloping of the inversion layer was present as seen in a decrease in the boundary-layer height to the north. The horizontal temperature gradient and sloping inversion across the ice edge are known to produce low-level baroclinicity, resulting in low-level jets (Brümmer, 1996; Chechin et al., 2013; Chechin and Lüpkes, 2017) and breeze-like circulations (Glendening and Burk, 1992). A low-level jet that might be related to an ice breeze was indeed present in the *Polar 6* vertical profiles with the

largest wind speed of up to 16 m s^{−1}. The increase in the near-surface wind across the ice edge was also observed at *Polarstern*. It is hard to identify the main mechanism of the low-level jet because the tip jet was also located over the ice edge. Nevertheless, as shown by Chechin and Lüpkes (2017), the increase in temperature and decrease in the inversion height in the north–south direction increase the easterly component of the low-level geostrophic wind. Thus, it might be possible that the observed easterly low-level jet was produced by a combination of the orographic and baroclinic factors.

3.4 Orographic wind dynamics

Elvidge et al. (2016) showed that different flow regimes over the Antarctic Peninsula produce contrasting structures of lee-side warming. Namely, a nonlinear flow regime, characterized by a presence of nonlinear high-amplitude internal gravity waves and their breaking over the mountains, results in strong downslope windstorms and strong warming directly downwind of the ridge which does not propagate further downwind due to a hydraulic jump. In a linear regime, no hydraulic jump forms and warming is observed over a larger distance downwind of the ridge.

We calculated the Froude number Fr/Nh (where U is flow velocity, N is the Brunt–Väisälä frequency and h is mountain height) using mean U and N of the incoming flow (details in Appendix B) as a measure of flow linearity. The flow regime is well described by the linear theory for the Froude number larger than its critical value (usually taken as unity). A transition to the nonlinear regime occurs when the Froude number becomes smaller than critical (Markowski and Richardson, 2011).

The simulated temporal evolution of the orographic winds during the considered episode is shown in Fig. 10 together with the corresponding value of the Froude number (Fig. 10, center). The variations in the Froude number were associated with changes in the incoming flow (Fig. B1, Appendix B). At the beginning of the episode, when the incoming flow velocity was high, the elevated inversion was strong, the stratification of the lower layer was close to neutral (Fig. B1, Appendix B) and Fr was close to unity, the flow “easily” went over the obstacle. Downslope windstorm occurred on almost all western slopes of Svalbard, and in the north it even extended for some distance across the sea. The hydraulic jump, which can be identified by the sharp boundary between high-velocity and low-velocity zones, was not very pronounced at the beginning of the episode. Starting from 12:00 UTC on 30 May a wake began to form on the lee side of the mountains as the Froude number decreased. Gap winds were most pronounced at low values of Fr (18:00 UTC, 30 May–06:00 UTC, 31 May, and 1 June). According to the simulation results, the northern tip jet strength depended weakly on temporal variations in Fr ; the tip jet velocity was decreasing

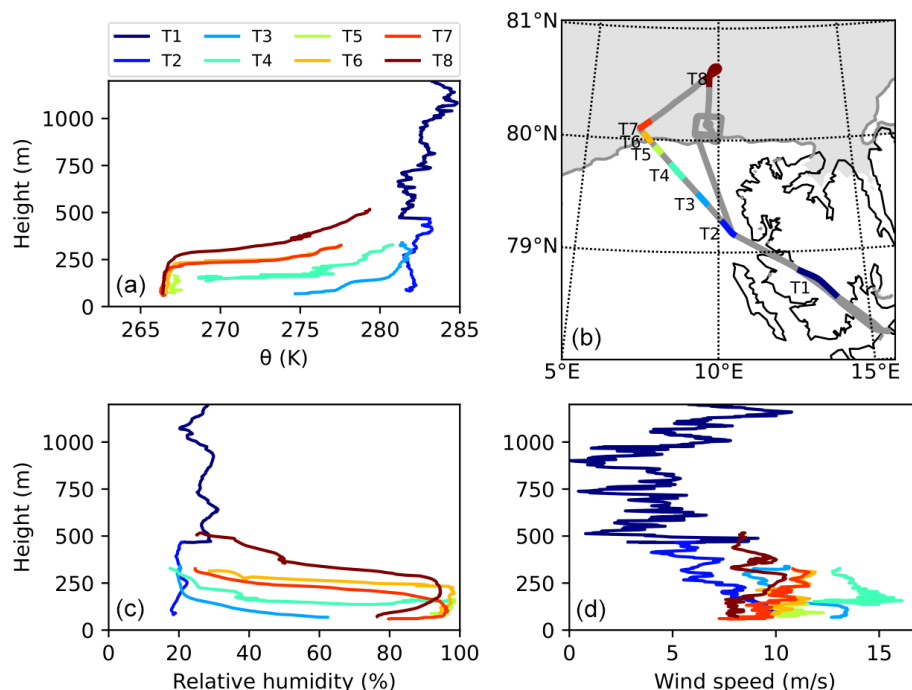


Figure 9. Vertical profiles of potential temperature (a), relative humidity (c) and wind speed (d) as observed by the *Polar 6* aircraft along its track line (b). Gray shading in panel (b) corresponds to the AMSR2 sea ice concentration larger than 50 % (<https://seaice.uni-bremen.de/>, last access: 25 January 2022).

during the considered episode due to the decrease in wind speed in the incoming flow (Fig. B1, Appendix B).

Unlike Elvidge et al. (2016), who considered two contrasting foehn cases, one of which was fully nonlinear (Fr from 0.15 to 0.4) and the other close to linear ($Fr \sim 1$), both regimes were observed during our episode. These two regimes are (1) downslope windstorm with a quasi-linear flow (high Froude number), propagating to some distance from the slope, with weakly pronounced gap flows and wake (06:00–12:00 UTC, 30 May), and (2) more amplified downslope windstorms with nonlinear flow (low Froude number), canyon effects and wakes, formed downstream of the hydraulic jumps (starting from 18:00 UTC, 30 May). In general, a decrease in Fr during the considered episode led to an increase in the intensity of downslope windstorms and to amplification of gap winds. Wind speed normalized by the incoming wind speed reached 2 on the lee side when $Fr < 0.8$ (Fig. 10). The incoming flow direction is also a crucial factor for the orographic flow dynamics. Namely, a downslope windstorm in the northwestern part of Svalbard occurred only at the beginning of the episode, when the wind direction was from the east and thus perpendicular to the main mountain ridge direction, while later the direction of the flow changed to northeasterly (Fig. B1).

During the considered episode we did not find a clear connection between the nonlinearity of the flow and the spread of foehn warming and its intensity. This can be explained, firstly, by a smaller variation in the Froude number

of the flow between the regimes as compared to Elvidge et al. (2016) and, secondly, by a more complex orography and also a variable wind direction in the incoming flow.

3.5 Surface heat budget in Ny-Ålesund and Adventdalen

In previous sections we showed that the effect of foehn over Spitsbergen was pronounced in air temperature, humidity and wind speed and also resulted in the absence of clouds. Thus, one would expect a strong impact of foehn on the components of the heat budget of the snow-covered land and glacier surface. The surface heat budget is expressed as

$$R + H + LE = B. \quad (1)$$

R is the radiative budget:

$$R = SW \downarrow - SW \uparrow + LW \downarrow - LW \uparrow, \quad (2)$$

where $SW \downarrow$ and $SW \uparrow$ are downward and upward shortwave radiation, respectively, and $LW \downarrow$ and $LW \uparrow$ are downward and upward longwave radiation, respectively.

H and LE are the turbulent sensible and latent heat fluxes, respectively, and B is the residual heat that is equal to the conductive heat flux to the snowpack (or ground) Q_D , which is further consumed by the snowmelt Q_{melt} when melting occurs. The latter is expressed as

$$Q_{\text{melt}} = L_i \rho_i \frac{\partial h}{\partial t}, \quad (3)$$

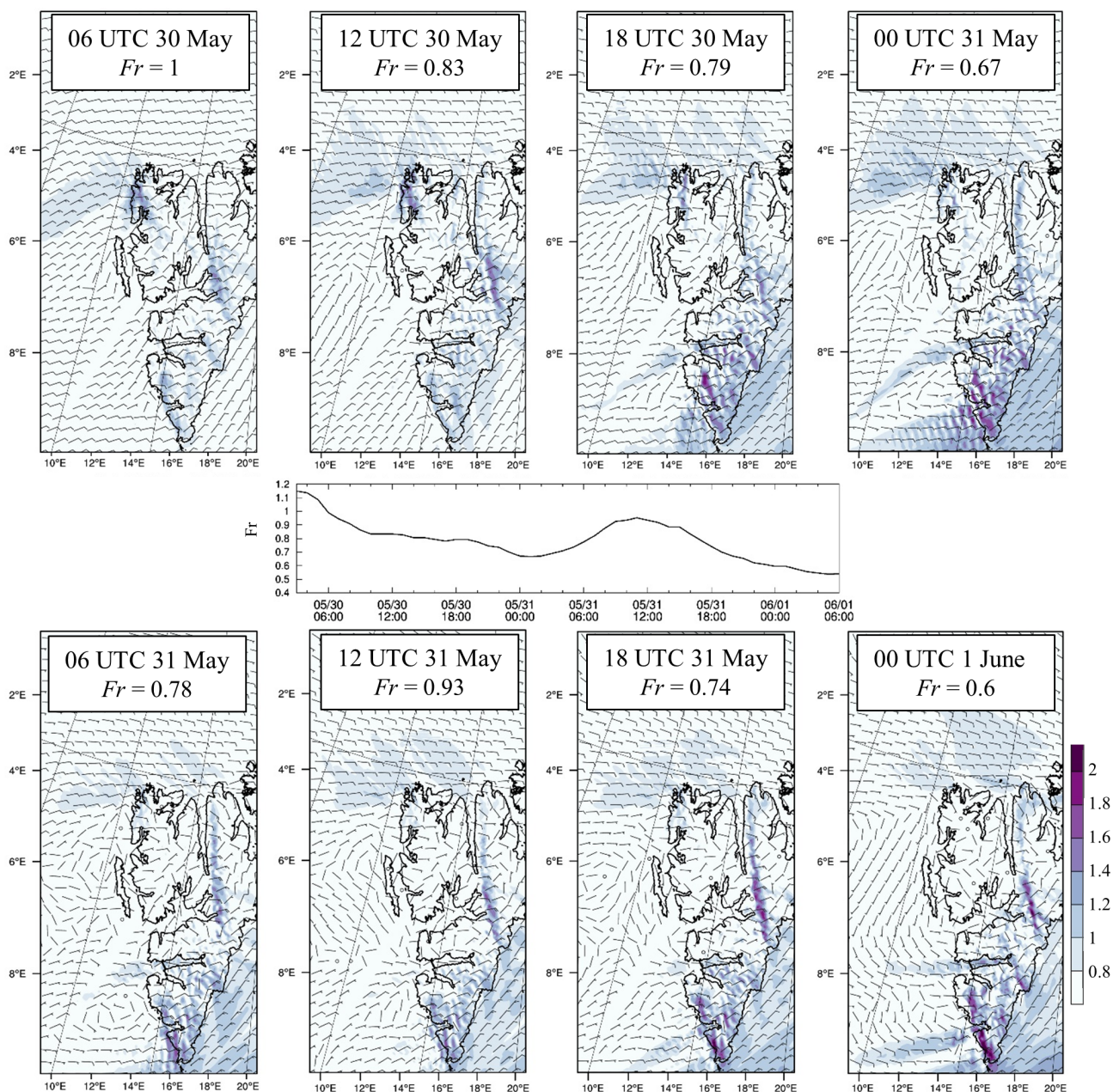


Figure 10. Dynamics of orographic flows during the observed foehn episode: wind speed (at 10 m a.g.l.) normalized to windward wind speed (averaged in the lowest 1.7 km layer at 80° N, 35° E (near Kvitøya)) (color) and wind direction (barbs) at 10 m a.g.l. and Fr number in the incoming flow (center panel) according to WRF modeling.

where L_i is specific heat of melting/freezing, ρ_i is snow/ice density and h is snow/ice thickness.

To obtain the budget in Adventdalen and Ny-Ålesund, LE and H were calculated from hourly averaged meteorological observations at two levels (2 and 10 m) in Adventdalen or from just one level (2 m) and from the surface in Ny-Ålesund

using the aerodynamic bulk formulae:

$$H = \rho C_p C_H \Delta U \Delta T, \quad (4)$$

$$LE = \rho L C_Q \Delta U \Delta q, \quad (5)$$

where C_p is specific heat at constant pressure; L is the specific heat of vaporization; and ΔU , ΔT and Δq are the wind speed, air temperature and specific humidity difference between two levels. The exchange coefficients are expressed

using Monin–Obukhov similarity theory as

$$C_H = C_Q = \frac{k^2}{\left[\ln\left(\frac{z}{z_{0m}}\right) - \Psi_M\left(\frac{z}{L}\right) + \Psi_M\left(\frac{z_{0m}}{L}\right) \right] \cdot \left[\ln\left(\frac{z}{z_{0r}}\right) - \Psi_H\left(\frac{z}{L}\right) + \Psi_H\left(\frac{z_{0r}}{L}\right) \right]}, \quad (6)$$

where k is the von Kármán constant and $\Psi_{M,H}$ are the universal stability functions for which the form obtained by Grachev et al. (2007) is used for stable stratification and the one obtained by Businger et al. (1971) and modified by Grachev et al. (2000) is used for unstable conditions. z_{0m} is the roughness length for momentum, and $z_{0r} = 0.1z_{0m}$ is the roughness length for T and q .

Equations (1)–(6) were applied to the available observations, and the results are shown for both stations in Fig. 11. Obviously, the surface heat budget was clearly dominated by the net shortwave radiation (yellow curves in Fig. 11a and b). The latter had a pronounced diurnal cycle and reached up to about 150 W m^{-2} in Ny-Ålesund and 500 W m^{-2} in Adventdalen during the daytime. In Ny-Ålesund, the radiation budget was smaller than in the Longyearbyen area primarily due to a much higher albedo (80 %–90 % in Ny-Ålesund and 40 %–50 % in Adventdalen). The reason for this large difference is that during the foehn event, albedo significantly decreased in Adventdalen (to 10 %–15 %, Fig. 11b) because the snow cover was partially eliminated there, as confirmed by a positive surface temperature on 31 May (Fig. 11f) which did not occur in Ny-Ålesund. It is known from previous studies that low albedo of 10 %–15 % is typical of the period just after the snowmelt in Adventdalen (Sjöblom, 2014). In Ny-Ålesund, the snow cover did not disappear as in Adventdalen, but the albedo of the snow-covered surface decreased to 60 %–80 % during the foehn episode.

The longwave radiative budget (magenta curves in Fig. 11a and b) was strongly negative during the foehn event and amounted to about -75 W m^{-2} at both sites. Such large values are clearly due to the low amount of water vapor in the air (caused by the large-scale advection of dry air mass and by foehn drying) and missing clouds.

As expected, turbulent heat fluxes during the foehn episode increased significantly (Fig. 11c and d), which is partly a result of the increased wind speed. Stratification of the surface layer was predominantly stable, with $0 < Ri_B < 0.2$ (where Ri_B is the bulk Richardson number) most of the time. Stable stratification was related to the advection of a warm air mass and the strong foehn effect. This is different from winter conditions when stable stratification is produced by the radiative cooling of the surface. Sensible heat fluxes with absolute values of up to 100 W m^{-2} were directed towards the surface, while the latent heat flux of up to 230 W m^{-2} in Adventdalen and 50 W m^{-2} in Ny-Ålesund was directed towards the atmosphere (Fig. 11c and d). The latent heat flux was 2–3 times larger than the sensible heat flux in Adventdalen. This is due to decreased relative humidity

Table 2. Melting and evaporation rates in Ny-Ålesund and Adventdalen, calculated from the heat budget.

	Melting rate, mm d^{-1} w.e.		Evaporation rate, mm d^{-1}	
	Ny-Ålesund	Adventdalen	Ny-Ålesund	Adventdalen
29 May	0.4	7.8	0.4	1.5
30 May	6.2	16.4	0.8	3.1
31 May	8.9	33.2	0.4	3.4

in the surface and boundary layer related to the foehn effect (Fig. 11d) and simultaneously high relative humidity at the surface due to snow melting and the evaporation of meltwater. In Ny-Ålesund, the relatively small latent heat flux was due to weak wind speed, though the relative humidity lowering in the surface layer was also well pronounced (Fig. 11c). The increase in evaporation and latent heat flux over a snow-covered surface during warm downslope windstorms is also known from other regions (e.g., Golding, 1978; MacDonald et al., 2012; Hayashi et al., 2005; Garvelmann et al., 2017). The daily average evaporation rate in Adventdalen, calculated from Eq. (4), ranges from 1.5 mm d^{-1} on 29 May (before foehn) to 3.4 mm d^{-1} on 31 May (during foehn), which is 1 order of magnitude greater than the evaporation rate in Ny-Ålesund (Table 2).

Using the calculated turbulent fluxes and the observed radiative budget, we calculated the residual term B (Fig. 11b, black line) (Eq. 1). It represents the heat flux related to the melting of snow/ice during ablation when surface temperature is near 0°C (from 30 May in Ny-Ålesund and on 29–30 May in Adventdalen) and heat flux to the ground after snow cover disappearance (only in Adventdalen). The positive surface temperature in Adventdalen on 31 May is explained by a partial (but not complete) degradation of the snow cover, which was noted from satellite images and webcams in Longyearbyen. Thus, the surface temperature, calculated from the upward longwave radiation flux, represented the average temperature of two surfaces – snow and soil. Therefore, the heat available for melting can also be calculated for 31 May in Adventdalen. At night, B was negative at both stations, while during the day the potential heat available for melting was large, especially on 31 May (Fig. 11a and b). The amount of melted snow can be estimated using Eq. (2) and the average snow density before the thawing season, which, according to measurements on Svalbard, is close to 400 kg m^{-3} (Gerland et al., 1999). In Adventdalen, the daily average melting rate grew from 7.8 (0.4) mm d^{-1} of water equivalent (w.e.) on 29 May to 33.2 (8.9) mm d^{-1} w.e. on 31 May in Adventdalen (Ny-Ålesund) (Table 2). The lower melting rate in Ny-Ålesund is explained, firstly, by a higher initial snow albedo (in Adventdalen, snow albedo was much lower most likely due to the previous melting periods and a more southerly position) and, secondly, by a significantly weaker wind than in Adventdalen. One should keep

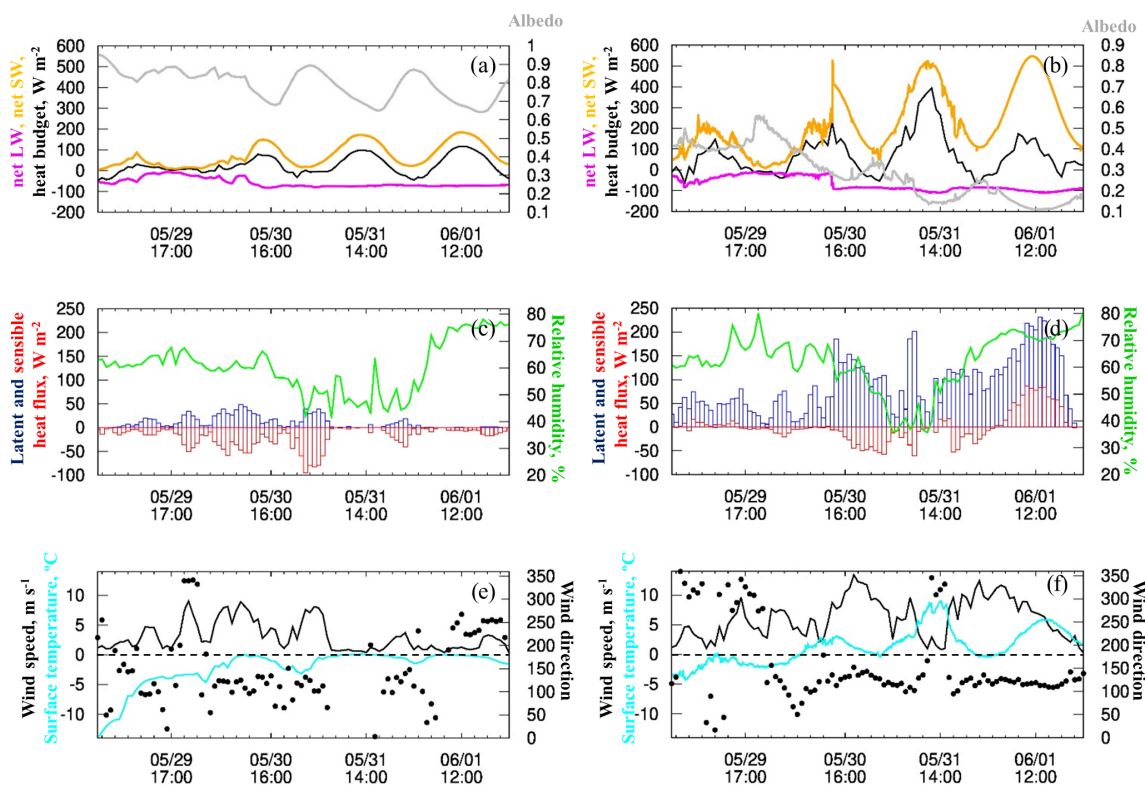


Figure 11. Terms of the radiation and heat budget in Ny-Ålesund (a, c, e) and Adventdalen (b, d, f) during 29 May–1 June 2017: (a, b) net shortwave (orange line) and net longwave (magenta line) radiation and residual term of heat budget (black line) and albedo (gray line), (c, d) turbulent heat fluxes (sensible (red boxes) and latent (blue boxes)) and relative humidity (green line) at 2 m a.g.l. (c) and 10 m a.g.l. (d), and (e, f) wind speed (black line) and direction (points) at 10 m a.g.l. and surface temperature (cyan line).

in mind that the estimated melting rate in Adventdalen on 31 May should be interpreted rather as the maximum value because, as noted before, the snow cover in Adventdalen had strongly degraded by that day. It is evident that the melting rate on 30–31 May was 1 order of magnitude greater than the evaporation rate (Table 2).

Thus, we found that most of the radiative budget as well as most of the turbulent sensible heat flux was consumed on phase transitions of water (snow melting, snow sublimation and evaporation). The amount of the available heat used for snowmelt was partially reduced by the large values of the turbulent latent heat flux. Thereby, foehn apparently has an effect on the water balance, especially in the Adventdalen region. The abundant and rapid snow melting should lead to a sharp increase in runoff. For example, summer melting due to foehns on Svalbard is often known to cause extreme river floods (Majchrowska et al., 2015). On the other hand, intense evaporation should lead to a decrease in runoff. For example, during foehn in the Alps, about half of the melting snow evaporates (Garvelmann et al., 2017). However, in our case, as in some other areas with foehns (Golding, 1978; MacDonald et al., 2012; Hayashi et al., 2005), evaporation plays a rather small role in the water balance of the snow cover, as it amounted to only 13 % of the melted snow in Adventdalen

and 8 % in Ny-Ålesund during the main melting period (30–31 May).

Finally, we surmise that even though the snowmelt would have probably occurred even without foehn, due to the synoptic advection of warm air, it was clearly accelerated by foehn in Ny-Ålesund and especially in Adventdalen. In particular, enhanced wind speed and air temperature and cloud clearance during foehn led to an increase in the surface radiative budget and the downward sensible heat flux. The latter two factors overwhelmed the heat loss due to sublimation and evaporation and thus provoked snow melting. It should be noted that in order to make more general conclusions on the effect of foehns on snowmelt and glacier mass balance, a much longer time series of observations has to be considered.

4 Conclusions

We presented the detailed analysis of the episode of an easterly flow over Svalbard which allowed us to investigate the main features of foehn and of the associated orographic flows and their impact on the structure of the surface and boundary layers. This was possible due to the availability of multiplatform observations obtained during the ALOUD/PASCAL campaigns. This analysis revealed a strong resemblance of

the considered foehn episode to other foehns, especially to foehn over the Antarctic Peninsula (Elvidge et al., 2015; Elvidge and Renfrew, 2016; Elvidge et al., 2016). The following results are obtained in this study:

1. A downslope windstorm on the western slopes of Svalbard at the end of May 2017 appeared in the form of foehn; that is, there was a significant increase in air temperature and a decrease in relative humidity on the lee side of the mountains. A typical foehn clearance in cloud cover was observed. Wind speed amplification during the downslope windstorm was observed over the leeward slopes or near the foot of the slopes. Foehn wind near the surface did not propagate downstream. On the contrary, the high-temperature and low-humidity effect of foehn reached far downstream into the sea, to a distance of more than 100 km from the coast (Fig. 5a).
2. Foehn led to a significant transformation of the boundary layer; the height and stratification of the boundary layer was largely determined by the downslope wind dynamics. A well-mixed layer was observed on the downwind side and over the fjords of western Svalbard. We suggest that it might have been produced both by the isentropic air descent and by the increased turbulence due to wave breaking. Below this well-mixed layer, a shallow stably stratified boundary layer formed over the snow surface and especially over the cold open sea. Foehn warming on the downwind side of Svalbard increased the horizontal temperature gradient across the sea ice edge in the Fram Strait. The temperature contrast between the northernmost profile over sea ice and in the lee of Svalbard reached 15 K. Baroclinicity associated with the horizontal temperature gradient might have affected the strength of the tip jet, which formed at the northern tip of Svalbard.
3. Gap winds, as well as tip jets, observed during the considered episode, differed from foehn by their larger horizontal extent (due to the absence of a hydraulic jump) and by the almost complete absence of warming in the surface layer (since the vertical air displacements were small). However, above the surface layer, the air was significantly warmer and drier, since the foehn effect spread over the whole leeward region of Svalbard.
4. Numerical modeling showed that the wind regimes of foehn and gap flows were determined by the flow direction and Froude number (Fr) in the incoming flow. Downslope wind amplification as well as gap flows was most prominent when Fr was less than 0.8, although for greater Fr values downslope, windstorms could propagate slightly further from the lee slope.
5. Foehn caused an intensification of the surface–atmosphere heat exchange in the Ny-Ålesund and

Longyearbyen (Adventdalen) regions, which accelerated the snowmelt and resulted in an almost complete disappearance of snow cover at the Adventdalen station. A large vertical gradient of specific humidity in the surface layer resulted in large values of latent heat flux. The latter formed due to the presence of snowmelt water and the air drying induced by foehn. The increased sensible heat flux directed from the atmosphere towards the surface partly compensated for air cooling due to evaporation. Thus, in accordance with Elvidge et al. (2016), melting during the foehn occurred primarily due to the large positive shortwave radiation budget and, secondly, due to the downward sensible heat flux, caused by the foehn warming.

6. To conclude, the presented analysis revealed the detailed structure of the foehn effect, downslope windstorms, gap flows and tip jets during easterly flow over Svalbard and their dependence on the incoming flow characteristics. The demonstrated acceleration of snowmelt during foehn suggests that the frequency of occurrence of an easterly flow in spring and summer might affect the glacier heat and mass budgets on the western side of Svalbard.

In general, the considered episode of an easterly wind in Svalbard had a characteristic spatial distribution of wind and temperature, as well as characteristic structure of the boundary layer, mentioned in many studies on the basis of both realistic and idealized simulations (Skeie and Grønås, 2000; Sandvik and Furevik, 2002; Dörnbrack et al., 2010; Reeve and Kolstad, 2011). Thus, our study based on an independent data set highlights the high degree of generality of these previous studies. Moreover, we hope that the results presented in this paper will be largely valid for other foehn episodes on Svalbard.

In this study, we did not involve the Lagrangian approach (widely used, for example, in Elvidge et al., 2016; Elvidge and Renfrew, 2016), though it can be very useful in analyzing various episodes of Svalbard foehns. Quantitative estimates of the contribution of turbulent fluxes to the evolution of the temperature and humidity of a Lagrangian volume during Svalbard foehns could be the subject of future research.

Appendix A: Underestimation of air temperature in WRF simulations

WRF consistently underestimated temperature (mean bias is -2.9 K) in the lower layers (surface and boundary layers) compared with observational data (Figs. A1, 3), though the model satisfactorily reproduced thermal stratification in most locations. This could be due to erroneous mixing in the boundary and surface layers in the model; however additional simulations with another boundary-layer parameterization (Asymmetric Convection Model 2, which is a hybrid

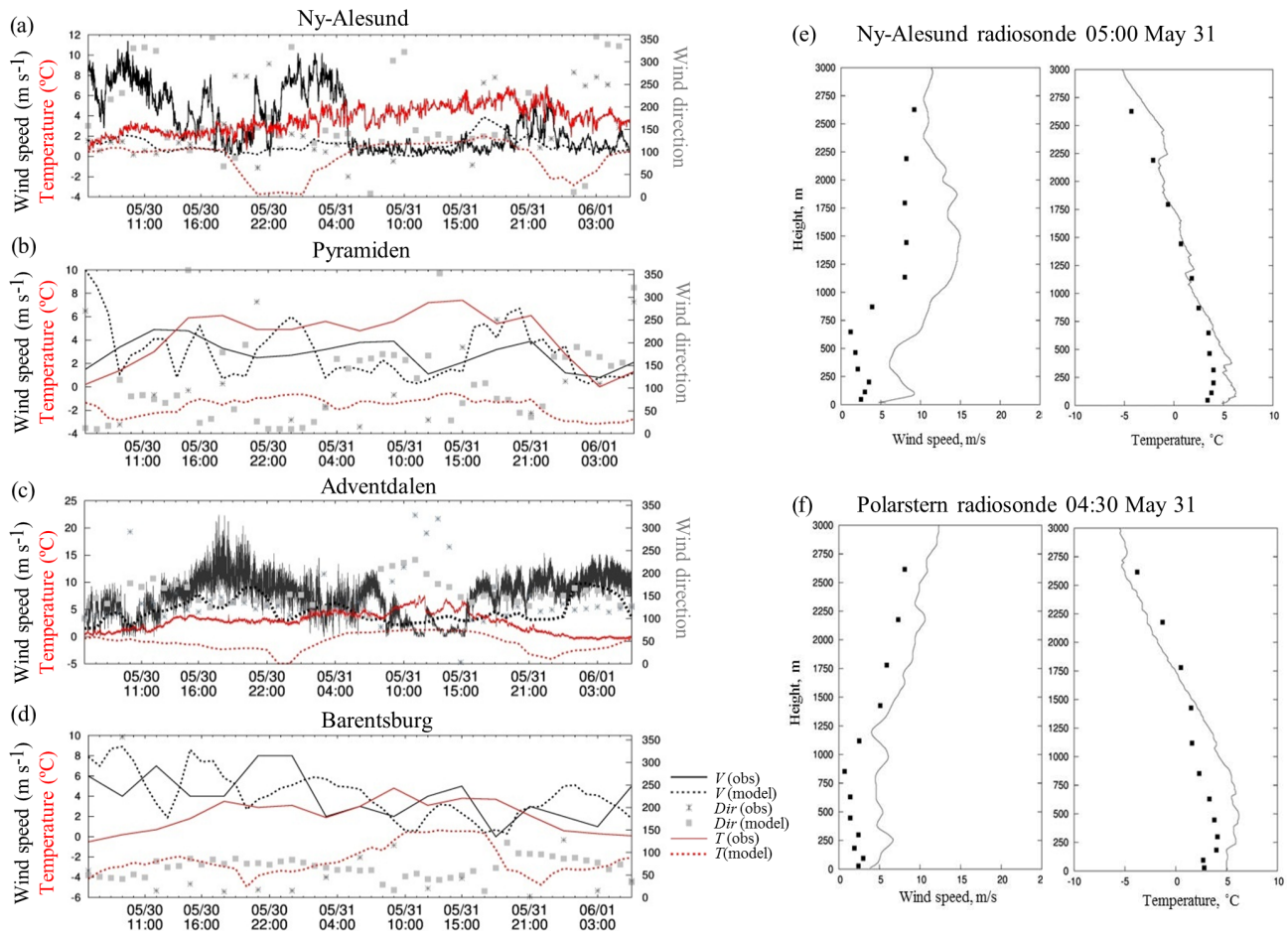


Figure A1. WRF model verification against AWS (a–d) and radiosonde data in Ny-Ålesund (e) and Polarstern (f). (a–d) 10 m wind speed V (black lines), 2 m temperature T (red lines) and wind direction Dir (asterisks and squares) according to AWS observations (solid lines and asterisks) and WRF simulation (dotted lines and squares). Wind speed at Adventdalen station was measured with a sonic anemometer at 2.7 m a.g.l. (e, f) Wind speed (left) and temperature (right) according to observations (solid line) and WRF simulation (squares).

non-local scheme in contrast to the local MYNN scheme) also failed to simulate surface temperature. The model also poorly reproduces the surface wind at some stations (for example, in Ny-Ålesund, the model erroneously simulates wake; Figs. A1, 5) due to the complexity of the orography and foehn wind dynamics. However, it is noteworthy that the model underestimated temperature not only at those stations where it incorrectly reproduced the wind regime but also at stations where the wind was reproduced correctly (e.g., Pyramiden, Adventdalen, Barentsburg – Fig. A1). Cloud cover was rather well reproduced by the model; therefore, the differences in the incoming radiation between the observations and the model were small (not shown), and this could not be the reason for the systematic temperature underestimation. We think, however, that these model difficulties do not affect our main conclusions because, e.g., the reproduction of stability is more important than the absolute values of temperature.

Appendix B: Incoming flow

The incoming flow is assumed to be unperturbed by the orography (i.e., without the influence of orographic waves and upstream blocking) on the windward side of an obstacle. To analyze the incoming flow, we used the profiles of wind speed and temperature (Fig. B1) at 80° N, 35° E (near Kvitøya) (point 1 in Fig. 7b), far enough from Svalbard not to be affected by blocking. To calculate the Froude number, we used U and N averaged in the lowest 1.7 km (maximum height of the mountain ridges) layer, and the prevailing mountain ridge height h was set as 1000 m. There is no consensus on over which layer to average U and N to calculate the Froude number; however, our previous study (Shestakova and Moiseenko, 2018) showed that the use of an average or maximum U did not significantly affect the results.

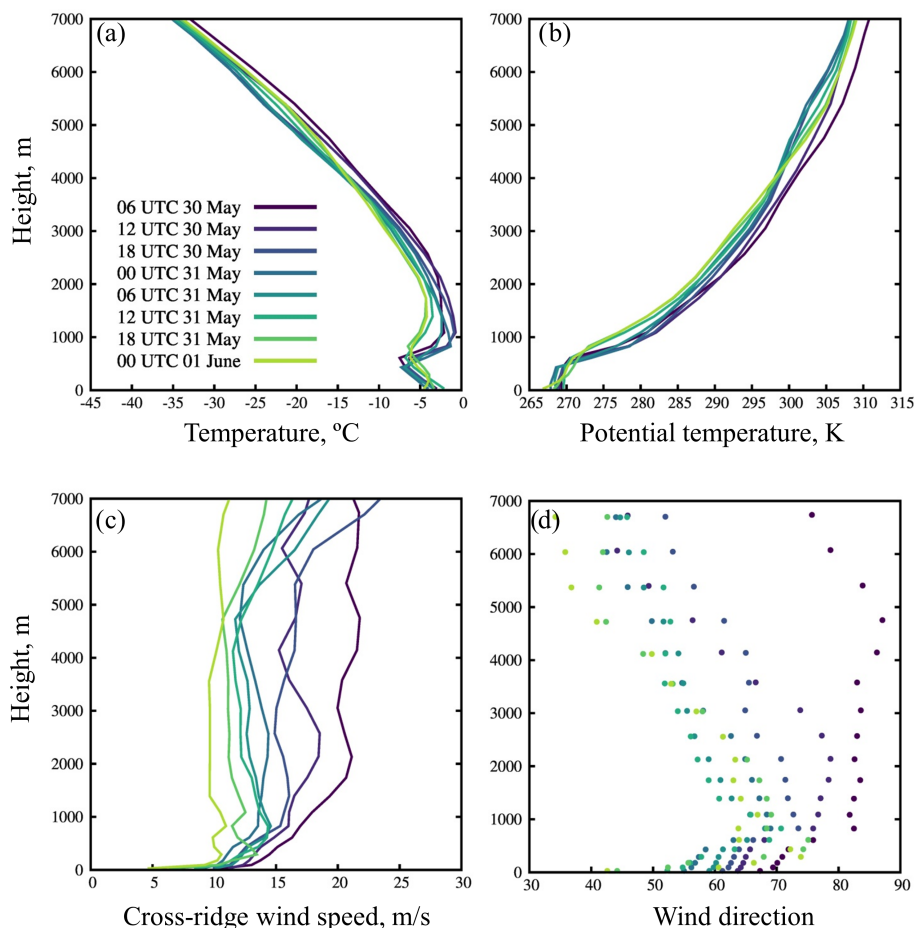


Figure B1. Vertical profiles of the incoming flow during the foehn episode according to WRF modeling: (a) air temperature, (b) potential temperature, (c) cross-ridge wind component and (d) wind direction.

Data availability. Surface meteorological observations in Ny-Ålesund are available in Maturilli (2018b; <https://doi.org/10.1594/PANGAEA.894599>). Surface radiation observations in Ny-Ålesund are available in Maturilli (2018a; <https://doi.org/10.1594/PANGAEA.887500>). Radiosounding observations in Ny-Ålesund are available in Maturilli (2017; <https://doi.org/10.1594/PANGAEA.879820>). Radiosounding observations on RV *Polarstern* are available in Schmithüsen (2017; <https://doi.org/10.1594/PANGAEA.882736>). *Polar 5* dropsonde observations are available in Ehrlich et al. (2019a; <https://doi.org/10.1594/PANGAEA.900204>). Aircraft observations during ALOUD are available in Ehrlich et al. (2019b). Surface meteorological and radiation observations in Adventdalen are available on the UNIS (the University Centre in Svalbard) website: <https://www.unis.no/resources/weather-stations/> (last access: 22 April 2021; UNIS, 2021). Archive meteorological data for other stations in Svalbard were obtained from the Yr website (a joint service by the Norwegian Meteorological Institute and the Norwegian Broadcasting Corporation): <https://www.yr.no/> (last access: 22 April 2021). GFS FNL analysis was obtained from the Research Data Archive (RDA), managed by the Data Engineering and Curation Section (DECS) of the Computational and Information Systems Laboratory

(CISL) at the National Center for Atmospheric Research (2000): <https://doi.org/10.5065/D6M043C6> (last access: 22 April 2021). The YOPP analysis of ECMWF (European Centre for Medium-Range Weather Forecasts) was obtained from the ECMWF website: <https://apps.ecmwf.int/datasets/data/yopp/levtype=sfc/type=cf/> (last access: 22 April 2021; ECMWF, 2021).

Author contributions. The main part of the paper was prepared by AAS and DGC. Data were provided by JH and MM. AAS, DGC, CL and MM discussed the results and contributed to the writing of the paper.

Competing interests. The contact author has declared that neither they nor their co-authors have any competing interests.

Disclaimer. The contents of this paper are solely the responsibility of the grantee and do not necessarily represent the official views of the supporting agencies.

Publisher's note: Copernicus Publications remains neutral with regard to jurisdictional claims in published maps and institutional affiliations.

Special issue statement. This article is part of the special issue “Arctic mixed-phase clouds as studied during the ACLOUD/PASCAL campaigns in the framework of (AC)³ (ACP/AMT/ESSD inter-journal SI)”. It is not associated with a conference.

Acknowledgements. The authors would like to acknowledge the ACLOUD/PASCAL campaigns participants for collecting the observational data used in this study. We acknowledge the use of imagery from the NASA Worldview application (<https://worldview.earthdata.nasa.gov>, last access: 25 January 2022), part of the NASA Earth Observing System Data and Information System (EOSDIS).

Financial support. This research was funded by the Deutsche Forschungsgemeinschaft (DFG, German Research Foundation) (project no. 268020496 TRR 172) within the Transregional Collaborative Research Center ArctiC Amplification: Climate Relevant Atmospheric and SurfaCe Processes, and Feedback Mechanisms (AC)³. The analysis of the orographic wind dynamics and the calculations of the surface heat budget terms were funded by the Russian Science Foundation (grant no. 18-77-10072). WRF modeling is supported by Russian Ministry of Science and Higher Education (grant no. 075-15-2019-1621).

Review statement. This paper was edited by Radovan Krejci and reviewed by two anonymous referees.

References

- Argentini, S., Viola, A. P., Mastrantonio, G., Maurizi, A., Georgiadis, T., and Nardino, M.: Characteristics of the boundary layer at Ny-Ålesund in the Arctic during the ARTIST field experiment, *Ann. Geophys.*, 46, 185–196, 2003.
- Barstad, I. and Adakudlu, M.: Observation and modelling of gap flow and wake formation on Svalbard, *Q. J. Roy. Meteor. Soc.*, 137, 1731–1738, 2011.
- Beine, H. J., Argentini, S., Maurizi, A., Mastrantonio, G., and Viola, A.: The local wind field at Ny-Ålesund and the Zeppelin mountain at Svalbard, *Meteorol. Atmos. Phys.*, 78, 107–113, 2001.
- Belusic, D., Pasarić, M., and Orlic, M.: Quasi-periodic bora gusts related to the structure of the troposphere, *Q. J. Roy. Meteor. Soc.*, 130, 1103–1121, 2004.
- Brinkmann, W. A.: Strong downslope winds at Boulder, Colorado, *Mon. Weather Rev.*, 102, 592–602, 1974.
- Brümmer, B.: Boundary-layer modification in wintertime cold-air outbreaks from the Arctic sea ice, *Bound.-Lay. Meteorol.*, 80, 109–125, 1996.
- Businger, J. A., Wyngaard, J. C., Izumi, Y., and Bradley, E. F.: Flux-profile relationships in the atmospheric surface layer, *J. Atmos. Sci.*, 28, 181–189, 1971.
- Chechin, D. G. and Lüpkes, C.: Boundary-layer development and low-level baroclinicity during high-latitude cold-air outbreaks: A simple model, *Bound.-Lay. Meteorol.*, 162, 91–116, 2017.
- Chechin, D. G., Lüpkes, C., Repina, I. A., and Gryanik, V. M.: Idealized dry quasi 2-D mesoscale simulations of cold-air outbreaks over the marginal sea ice zone with fine and coarse resolution, *J. Geophys. Res.-Atmos.*, 118, 8787–8813, 2013.
- Dethloff, K., Handorf, D., Jaiser, R., Rinke, A., and Klinghammer, P.: Dynamical mechanisms of Arctic amplification, *Ann. NY Acad. Sci.*, 1436, 184–194, 2019.
- Dörnbrack, A., Stachlewska, I. S., Ritter, C., and Neuber, R.: Aerosol distribution around Svalbard during intense easterly winds, *Atmos. Chem. Phys.*, 10, 1473–1490, <https://doi.org/10.5194/acp-10-1473-2010>, 2010.
- Doyle, J. D. and Shapiro, M. A.: Flow response to large-scale topography: The Greenland tip jet, *Tellus A*, 51, 728–748, 1999.
- Durrán, D. R.: Mountain waves and downslope winds, in: *Atmospheric processes over complex terrain*, edited by: Blumen, W., American Meteorological Society, Boston, MA, 59–81, https://doi.org/10.1007/978-1-935704-25-6_4, 1990.
- ECMWF: Data archive of global meteorological fields from ECMWF Integrated Forecast System for the Year of Polar Prediction, ECMWF [data set], <https://apps.ecmwf.int/datasets/data/yopp/levtype=sfc/type=cf/>, last access: 22 April 2021.
- Efimov, V. V. and Barabanov, V. S.: Gustiness of the Novorossiysk bora, *Russ. Meteorol. Hydro.*, 38, 840–845, 2013.
- Efimov, V. V. and Komarovskaya, O. I.: Numerical simulation of the Novaya Zemlya bora, *Russ. Meteorol. Hydro.*, 43, 22–28, 2018.
- Ehrlich, A., Stapf, J., Lüpkes, C., Mech, M., Crewell, S., and Wendisch, M.: Meteorological measurements by dropsondes released from POLAR 5 during ACLOUD 2017, PANGAEA [data set], <https://doi.org/10.1594/PANGAEA.900204>, 2019a.
- Ehrlich, A., Wendisch, M., Lüpkes, C., Buschmann, M., Bozem, H., Chechin, D., Clemen, H.-C., Dupuy, R., Eppers, O., Hartmann, J., Herber, A., Jäkel, E., Järvinen, E., Jourdan, O., Kästner, U., Kliesch, L.-L., Köllner, F., Mech, M., Mertes, S., Neuber, R., Ruiz-Donoso, E., Schnaiter, M., Schneider, J., Stapf, J., and Zanatta, M.: A comprehensive in situ and remote sensing data set from the Arctic CLOUD Observations Using airborne measurements during polar Day (ACLOUD) campaign, *Earth Syst. Sci. Data*, 11, 1853–1881, <https://doi.org/10.5194/essd-11-1853-2019>, 2019b.
- Elvidge, A. D. and Renfrew, I. A.: The causes of foehn warming in the lee of mountains, *B. Am. Meteorol. Soc.*, 97, 455–466, 2016.
- Elvidge, A. D., Renfrew, I. A., King, J. C., Orr, A., Lachlan-Cope, T. A., Weeks, M., and Gray, S. L.: Foehn jets over the Larsen C ice shelf, Antarctica, *Q. J. Roy. Meteor. Soc.*, 141, 698–713, 2015.
- Elvidge, A. D., Renfrew, I. A., King, J. C., Orr, A., and Lachlan-Cope, T. A.: Foehn warming distributions in nonlinear and linear flow regimes: A focus on the Antarctic Peninsula, *Q. J. Roy. Meteor. Soc.*, 142, 618–631, 2016.
- Elvidge, A. D., Munneke, P. K., King, J. C., Renfrew, I. A., and Gilbert, E.: Atmospheric drivers of melt on Larsen C Ice Shelf: Surface energy budget regimes and the impact of foehn, *J. Geophys. Res.-Atmos.*, 125, e2020JD032463, <https://doi.org/10.1029/2020JD032463>, 2020.

- Gaberšek, S. and Durran, D. R.: Gap flows through idealized topography. Part I: Forcing by large-scale winds in the nonrotating limit, *J. Atmos. Sci.*, 61, 2846–2862, 2004.
- Garvelmann, J., Fersch, B., Kopp, M., Rieger, W., and Kunstmann, H.: Snow evaporation quantification during a Foehn event in a subalpine environment, *EGU General Assembly Conference Abstracts*, 23–28 April 2017, Vienna, Austria, 19, 13600, <https://doi.org/10.13140/RG.2.2.33473.45926>, 2017.
- Gerland, S., Winther, J. G., Børre Ørbæk, J., and Ivanov, B. V.: Physical properties, spectral reflectance and thickness development of first year fast ice in Kongsfjorden, Svalbard, *Polar Res.*, 18, 275–282, 1999.
- Glendening, J. W. and Burk, S. D.: Turbulent transport from an Arctic lead: A large-eddy simulation, *Bound.-Lay. Meteorol.*, 59, 315–339, 1992.
- Golding, D. L.: Calculated snowpack evaporation during Chinooks along the eastern slopes of the Rocky Mountains in Alberta, *J. Appl. Meteorol.*, 17, 1647–1651, 1978.
- Grachev, A. A., Fairall, C. W., and Bradley, E. F.: Convective profile constants revisited, *Bound.-Lay. Meteorol.*, 94, 495–515, 2000.
- Grachev, A. A., Andreas, E. L., Fairall, C. W., Guest, P. S., and Persson, P. O. G.: SHEBA flux–profile relationships in the stable atmospheric boundary layer, *Bound.-Lay. Meteorol.*, 124, 315–333, 2007.
- Hayashi, M., Hirota, T., Iwata, Y., and Takayabu, I.: Snowmelt energy balance and its relation to foehn events in Tokachi, Japan, *J. Meteorol. Soc. Jpn.* II, 83, 783–798, 2005.
- Hoinka, K. P.: Observation of the airflow over the Alps during a foehn event, *Q. J. Roy. Meteor. Soc.*, 111, 199–224, 1985.
- Hughes, M. and Cassano, J. J.: The climatological distribution of extreme Arctic winds and implications for ocean and sea ice processes, *J. Geophys. Res.-Atmos.*, 120, 7358–7377, 2015.
- Iacono, M. J., Delamere, J. S., Mlawer, E. J., Shephard, M. W., Clough, S. A., and Collins, W. D.: Radiative forcing by long-lived greenhouse gases: Calculations with the AER radiative transfer models, *J. Geophys. Res.*, 113, D13103, <https://doi.org/10.1029/2008JD009944>, 2008.
- Kilpeläinen, T. and Sjöblom, A.: Momentum and sensible heat exchange in an ice-free Arctic fjord, *Bound.-Lay. Meteorol.*, 134, 109–130, 2010.
- Kilpeläinen, T., Vihma, T., Lafsson, H. O., and Karlsson, P. E.: Modelling of spatial variability and topographic effects over Arctic fjords in Svalbard, *Tellus A*, 63, 223–237, 2011.
- Klemp, J. B. and Lilly, D. K.: The dynamics of wave-induced downslope winds, *J. Atmos. Sci.*, 32, 320–339, 1975.
- Knudsen, E. M., Heinold, B., Dahlke, S., Bozem, H., Crewell, S., Gorodetskaya, I. V., Heygster, G., Kunkel, D., Maturilli, M., Mech, M., Viceto, C., Rinke, A., Schmithüsen, H., Ehrlich, A., Macke, A., Lüpkes, C., and Wendisch, M.: Meteorological conditions during the ALOUD/PASCAL field campaign near Svalbard in early summer 2017, *Atmos. Chem. Phys.*, 18, 17995–18022, <https://doi.org/10.5194/acp-18-17995-2018>, 2018.
- Knust, R.: Polar Research and Supply Vessel *POLARSTERN* Operated by the Alfred-Wegener-Institute, *J. Large-Scale Res. Facilities*, 3, A119, <https://doi.org/10.17815/jlsrf-3-163>, 2017.
- Láska, K., Chládková, Z., and Hošek, J.: High-resolution numerical simulation of summer wind field comparing WRF boundary-layer parametrizations over complex Arctic topography: case study from central Spitsbergen, *Meteorol. Z.*, 26, 391–408, 2017.
- MacDonald, M. K., Essery, R. L. H., and Pomeroy, J. W.: Effects of Chinook winds (foehn) on snow cover in western Canada, *EGU General Assembly Conference Abstracts*, 22–27 April, 2012, Vienna, Austria, 14, 13690, 2012.
- Maciejowski, W. and Michniewski, A.: Variations in weather on the east and west coasts of South Spitsbergen, Svalbard, *Polish Polar Res.*, 28, 123–136, 2007.
- Majchrowska, E., Ignatiuk, D., Jania, J., Marszałek, H., and Waśnik, M.: Seasonal and interannual variability in runoff from the Werenskioldbreen catchment, Spitsbergen, *Polish Polar Res.*, 36, 197–224, 2015.
- Mäkiranta, E., Vihma, T., Sjöblom, A., and Tastula, E. M.: Observations and modelling of the atmospheric boundary layer over sea-ice in a Svalbard Fjord, *Bound.-Lay. Meteorol.*, 140, 105–123, 2011.
- Markowski, P. and Richardson, Y.: Mesoscale meteorology in mid-latitudes, in: *Advances in Weather and Climate*, edited by: Inness, P. and Beasley, W., John Wiley & Sons, 2, 407 pp., <https://doi.org/10.1002/9780470682104>, 2011.
- Maturilli, M.: High resolution radiosonde measurements from station Ny-Ålesund (2017–05), Alfred Wegener Institute – Research Unit Potsdam, PANGAEA [data set], <https://doi.org/10.1594/PANGAEA.879820>, 2017.
- Maturilli, M.: Basic and other measurements of radiation at station Ny-Ålesund (2017–05), Alfred Wegener Institute – Research Unit Potsdam, PANGAEA [data set], <https://doi.org/10.1594/PANGAEA.887500>, 2018a.
- Maturilli, M.: Continuous meteorological observations at station Ny-Ålesund (2017–05), Alfred Wegener Institute – Research Unit Potsdam, PANGAEA [data set], <https://doi.org/10.1594/PANGAEA.894599>, 2018b.
- Maturilli, M., Herber, A., and König-Langlo, G.: Climatology and time series of surface meteorology in Ny-Ålesund, Svalbard, *Earth Syst. Sci. Data*, 5, 155–163, <https://doi.org/10.5194/essd-5-155-2013>, 2013.
- Miگاła, K., Nasiółkowski, T., and Pereyma, J.: Topoclimatic conditions in the Hornsund area (SW Spitsbergen) during the ablation season 2005, *Polish Polar Res.*, 29, 73–91, 2008.
- Nakanishi, M. and Niino, H.: Development of an improved turbulence closure model for the atmospheric boundary layer, *J. Meteor. Soc. Japan*, 87, 895–912, 2009.
- National Centers for Environmental Prediction/National Weather Service/NOAA/U.S. Department of Commerce: NCEP FNL Operational Model Global Tropospheric Analyses, continuing from July 1999, Research Data Archive at the National Center for Atmospheric Research, Computational and Information Systems Laboratory [data set], <https://doi.org/10.5065/D6M043C6>, 2000, updated daily.
- Olafsson, H.: The heat source of the foehn, *Hrvatski Meteorološki časopis*, 40, 542–545, 2005.
- Outten, S. D., Renfrew, I. A., and Petersen, G. N.: An easterly tip jet off Cape Farewell, Greenland. Part II: Simulations and dynamics, *Q. J. Roy. Meteor. Soc.*, 135, 1934–1949, 2009.
- Reeve, M. A. and Kolstad, E. W.: The Spitsbergen south cape tip jet, *Q. J. Roy. Meteor. Soc.*, 137, 1739–1748, 2011.
- Renfrew, I. A., Outten, S. D., and Moore, G. W. K.: An easterly tip jet off Cape Farewell, Greenland. Part I: Aircraft observations, *Q. J. Roy. Meteor. Soc.*, 135, 1919–1933, 2009.

- Samuelsen, E. M. and Graverson, R. G.: Weather situation during observed ship-icing events off the coast of Northern Norway and the Svalbard archipelago, *Weather Climate Extremes*, 24, 100200, <https://doi.org/10.1016/j.wace.2019.100200>, 2019.
- Sandvik, A. D. and Furevik, B. R.: Case study of a coastal jet at Spitsbergen – Comparison of SAR-and model-estimated wind, *Mon. Weather Rev.*, 130, 1040–1051, 2002.
- Schmithüsen, H.: Upper air soundings during *POLARSTERN* cruise PS106/1 (ARK-XXXI/1.1), Alfred Wegener Institute, Helmholtz Centre for Polar and Marine Research, Bremerhaven, PANGAEA [data set], <https://doi.org/10.1594/PANGAEA.882736>, 2017.
- Seibert, P.: South foehn studies since the ALPEX experiment, *Meteorol. Atmos. Phys.*, 43, 91–103, 1990.
- Serreze, M. C. and Barry, R. G.: Processes and impacts of Arctic amplification: A research synthesis, *Global Planet. Change*, 77, 85–96, 2011.
- Shestakova, A. A. and Moiseenko, K. B.: Hydraulic regimes of flow over mountains during severe downslope windstorms: Novorossiysk bora, Novaya Zemlya bora, and Pevek Yuzhak, *Izvestiya, Atmos. Ocean. Phys.*, 54, 344–353, 2018.
- Shestakova, A. A., Toropov, P. A., Stepanenko, V. M., Sergeev, D. E., and Repina, I. A.: Observations and modelling of downslope windstorm in Novorossiysk, *Dynam. Atmos. Oceans*, 83, 83–99, 2018.
- Shestakova, A. A., Toropov, P. A., and Matveeva, T. A.: Climatology of extreme downslope windstorms in the Russian Arctic, *Weather Climate Extremes*, 28, 100256, <https://doi.org/10.1016/j.wace.2020.100256>, 2020.
- Sjöblom, A.: Turbulent fluxes of momentum and heat over land in the High-Arctic summer: the influence of observation techniques, *Polar Res.*, 33, 21567, <https://doi.org/10.3402/polar.v33.21567>, 2014.
- Skeie, P. and Grønås, S.: Strongly stratified easterly flows across Spitsbergen, *Tellus A*, 52, 473–486, 2000.
- Steinhoff, D. F., Bromwich, D. H., and Monaghan, A.: Dynamics of the foehn mechanism in the McMurdo Dry Valleys of Antarctica from Polar WRF, *Q. J. Roy. Meteor. Soc.*, 139, 1615–1631, 2013.
- Turton, J. V., Kirchgaessner, A., Ross, A. N., and King, J. C.: The spatial distribution and temporal variability of föhn winds over the Larsen C ice shelf, Antarctica, *Q. J. Roy. Meteor. Soc.*, 144, 1169–1178, 2018.
- UNIS: UNIS Weather stations and CTD stations, UNIS [data set], available at: <https://www.unis.no/resources/weather-stations/>, last access: 22 April 2021.
- Wendisch, M., Macke, A., Ehrlich, A., Lüpkes, C., Mech, M., Chechin, D., Dethloff, K., Barrientos Velasco, C., Bozem H., Brückner, M., Clemen, H.-C., Crewell, S., Donth, T., Dupuy, R., Ebell, K., Egerer, U., Engelmann, R., Engler, C., Eppers, O., Gehrmann, M., Gong, X., Gottschalk, M., Gourbeyre, C., Griesche, H., Hartmann, J., Hartmann, M., Heinold, B., Herber, A., Herrmann, H., Heygster, G., Hoor, P., Jafariserajehlou, S., Jäkel, E., Järvinen, E., Jourdan, O., Kästner, U., Kecorius, S., Knudsen, E. M., Köllner, F., Kretzschmar, J., Lelli, L., Leroy, D., Maturilli, M., Mei, L., Mertes, S., Mioche, G., Neuber, R., Nicolaus, M., Nomokonova, T., Notholt, J., Palm, M., van Pinxteren, M., Quaas, J., Richter, P., Ruiz-Donoso, E., Schäfer, M., Schmieder, K., Schnaiter, M., Schneider, J., Schwarzenböck, A., Seifert, P., Shupe, M.D., Siebert, H., Spreen, G., Stapf, J., Stratmann, F., Vogl, T., Welti, A., Wex, H., Wiedensohler, A., Zannata, M., and Zeppenfeld, S.: The Arctic cloud puzzle: Using ACLOUD/PASCAL multiplatform observations to unravel the role of clouds and aerosol particles in arctic amplification, *B. Am. Meteorol. Soc.*, 100, 841–871, 2019.